AIAA JOURNAL
Vol. 47, No. 11, November 2009

High-Fidelity Simulation of Transitional Flows past a Plunging Airfoil

Miguel R. Visbal*
U.S. Air Force Research Laboratory, Wright-Patterson Air Force Base, Ohio 45433

DOI: 10.2514/1.43038

This investigation addresses the simulation of the unsteady separated flows encountered by a plunging airfoil under low-Reynolds-number conditions ($Re_c \leq 6 \times 10^4$). The flowfields are computed employing an extensively validated high-fidelity implicit large-eddy simulation approach. Calculations are performed first for a SD7003 airfoil section at an angle of attack $\alpha_o = 4\,\mathrm{deg}$ plunging with reduced frequency $k = 3.93$ and amplitude $h_o/c = 0.05$. Under these conditions, it is demonstrated that, for $Re_c = 10^4$, transitional effects are not significant. For $Re_c = 4 \times 10^4$, the dynamic-stall vortex system is laminar at its inception, however, shortly afterward, it experiences an abrupt breakdown due to the onset of spanwise instabilities. A description of this transition process near the leading edge is provided. As a second example, the suppression of stall at high angle of attack ($\alpha_o = 14\,\mathrm{deg}$) is investigated using high-frequency, small-amplitude vibrations ($k = 10$, $h_o/c = 0.005$). At $Re_c = 6 \times 10^4$, separation is completely eliminated in a time-averaged sense, and the mean drag is reduced by approximately 40%. For larger forcing amplitude ($h_o/c = 0.04$, $Re_c = 10^4$), a very intriguing regime emerges. The dynamic-stall vortex moves around and in front of the leading edge and experiences a dramatic breakdown as it impinges against the airfoil. The corresponding phased-averaged flow displays no coherent vortices propagating along the airfoil upper surface. This new flow structure is also characterized in the mean by the existence of a strong jet in the near wake which produces net thrust. This study demonstrates the importance of transition for low-Reynolds-number maneuvering airfoils and the suitability of the implicit large-eddy simulation approach for exploring such flow regime.

I. Introduction

UNSTEADY low-Reynolds-number flows are found in natural flyers, as well as in small unmanned air vehicles and micro air vehicles (or MAVs) due to the relatively small size and low flying speeds involved [1,2]. Depending upon the specific conditions, these flowfields may be characterized by extensive regions of laminar flow, by the onset of laminar separation bubbles (even at moderate incidence), and by laminar–turbulent transition zones. For the case of flapping wings, as well as for severe gusts, the highly unsteady forcing induces the formation of dynamic-stall-like vortices whose evolution and interaction with the aerodynamic surfaces have a significant impact on flight stability and performance. Although much has been studied about these unsteady vortical flow features, challenges still remain in understanding their structure, scaling, and implications on flight efficiency, in particular over the broad range of parameters encountered.

From the perspective of analysis and simulation, this nontraditional low-Reynolds-number aerodynamic regime over flapping surfaces poses a severe challenge due to several factors. Difficulties arise by the presence of highly unsteady flows which defy standard quasi-steady characterization. The flowfields are of a mixed laminar-transitional-turbulent type for which high-Reynolds-number analysis tools may not be adequate. Both in nature and in MAV applications, an extensive range of parameters and configurations are encountered. Lastly, for lightweight flexible vehicles, there exists a strong coupling of the unsteady aerodynamics and structural response which requires advanced multidisciplinary approaches. Given the aforementioned difficulties, a hierarchy of increasingly complex canonical model problems can be considered to facilitate progress in the improved understanding and prediction of the physics relevant to small fliers. The simplest of these configurations is a maneuvering airfoil section which has motivated recent experiments and computations of low-Reynolds-number airfoils under both static and dynamic conditions [3–7].

As a point of departure in this research direction, the present work investigates the application of an implicit large-eddy simulation (ILES) approach for the prediction of transitional flows about plunging airfoils. This ILES approach, previously introduced in [8,9], is based on high-order compact schemes for the spatial derivatives and on a Pade-type low-pass filter to ensure stability. The high-order scheme is essential for the accuracy demanded by the transition process, whereas the discriminating low-pass filter operator provides regularization in turbulent flow regions in lieu of a standard subgrid-scale (SGS) model. This method is particularly attractive for the present application wherein a seamless approach capable of handling mixed laminar, transitional, and turbulent flows is needed.

Results are presented for flow over a plunging SD7003 airfoil section, a geometry which has been considered recently in several experimental and computational studies [4–7]. Due in part to the availability of experimental data, as well as to computational requirements, we investigate initially the case of fairly high reduced frequencies and small plunging amplitudes. Low-frequency, large-amplitude cases of more relevance to flapping flight will be reported in a follow-up study.

In this paper, two different situations are examined for the plunging SD7003 airfoil. In the first category, the airfoil is set at a small static angle of attack $\alpha_o = 4\,\mathrm{deg}$, and the imposed reduced frequency and nondimensional plunging amplitude are $k = \pi f c/U_\infty = 3.93$ and $h_o = \hat{h}_o/c = 0.05$, respectively. These parameters result in a maximum excursion in induced angle of attack of 21.5 deg. To explore the impact of transition on the flow structure around the plunging airfoil, several Reynolds numbers are considered ranging from $Re_c = \rho U_\infty c/\mu = 10^3$ to 4×10^4. Emphasis is placed on the results for $Re_c = 10^4$ and $Re_c = 4 \times 10^4$ corresponding to the recent particle image velocimetry (PIV) measurements of [7]. Similar experimental studies for a NACA 0012 airfoil performing either

Presented as Paper 391 at the 47th AIAA Aerospace Sciences Meeting, Orlando, FL, 5–8 January 2009; received 2 January 2009; revision received 15 July 2009; accepted for publication 17 July 2009.

*Technical Area Leader, Computational Sciences Branch, Air Vehicles Directorate. Associate Fellow AIAA.

plunging or pitching small-amplitude, high-frequency oscillations have also been provided in [10,11], with emphasis on the wake structure and thrust generation mechanisms.

The second category of simulations addresses the suppression of stall at high angle of attack ($\alpha_o = 14\,\text{deg}$) employing very high-frequency, small-amplitude plunging oscillations. The prescribed reduced frequency is $k = 10$ and the corresponding plunging amplitude ranged from $h_o = 0.005$ to 0.04. Two different values of Reynolds number ($Re_c = 10^4$ and 6×10^4) are considered to explore the effects of transition. Stall suppression by means of high-frequency plunging motion has also been investigated independently and for a different airfoil section in the experimental study of [12].

For both types of plunging cases noted here, the unsteady flowfields are characterized by the formation of leading-edge dynamic-stall vortices [13] due to the large motion-induced angle of attack. Numerous two-dimensional computational studies have appeared in the literature regarding the dynamic-stall vortex formation under laminar, transitional, and turbulent conditions [14–18]. For high-Reynolds-number flows, these approaches have traditionally employed a hierarchy of turbulence models augmented in some instances with empirical transition predictions. Unlike those previous studies, the present investigation addresses for the first time the direct numerical simulation of the full three-dimensional transitional dynamic-stall vortex evolution albeit at low Reynolds number relevant to MAV systems. It is demonstrated that, although the incipient separation and dynamic-stall vortex formation are initially laminar, the subsequent abrupt onset of transition plays a critical role even at modest Reynolds numbers.

The overall objectives of this investigation can be summarized as follows: 1) demonstration of the suitability of the ILES approach for transitional low-Reynolds-number unsteady flows pertinent to MAVs, 2) elucidation of the three-dimensional structure of the dynamic-stall vortex system for a range of parameters, 3) exploration of stall suppression by means of high-frequency, small-amplitude vibrations, 4) detailed comparison with available experimental PIV measurements [7], and 5) comparison of 2-D and 3-D simulations in terms of overall flow structure and aerodynamic loads.

II. Governing Equations

For these maneuvering airfoil simulations, the governing equations are the unfiltered full compressible Navier–Stokes equations cast in strong conservative form after introducing a general time-dependent curvilinear coordinate transformation $(x, y, z, t) \rightarrow (\xi, \eta, \zeta, \tau)$ [19,20] from physical to computational space. In terms of nondimensional variables, these equations can be written in vector notation as

$$\frac{\partial}{\partial \tau}\left(\frac{\mathbf{U}}{J}\right) + \frac{\partial \hat{F}}{\partial \xi} + \frac{\partial \hat{G}}{\partial \eta} + \frac{\partial \hat{H}}{\partial \zeta} = \frac{1}{Re}\left[\frac{\partial \hat{F}_v}{\partial \xi} + \frac{\partial \hat{G}_v}{\partial \eta} + \frac{\partial \hat{H}_v}{\partial \zeta}\right] \quad (1)$$

where $\mathbf{U} = \{\rho, \rho u, \rho v, \rho w, \rho E\}$ denotes the solution vector, $J = \partial(\xi, \eta, \zeta, \tau)/\partial(x, y, z, t)$ is the transformation Jacobian, and $\hat{F}$, $\hat{G}$, and $\hat{H}$ are the inviscid fluxes given by

$$\hat{F} = \begin{bmatrix} \rho\hat{U} \\ \rho u\hat{U} + \hat{\xi}_x p \\ \rho v\hat{U} + \hat{\xi}_y p \\ \rho w\hat{U} + \hat{\xi}_z p \\ (\rho E + p)\hat{U} - \hat{\xi}_t p \end{bmatrix} \quad (2)$$

$$\hat{G} = \begin{bmatrix} \rho\hat{V} \\ \rho u\hat{V} + \hat{\eta}_x p \\ \rho v\hat{V} + \hat{\eta}_y p \\ \rho w\hat{V} + \hat{\eta}_z p \\ (\rho E + p)\hat{V} - \hat{\eta}_t p \end{bmatrix} \quad (3)$$

$$\hat{H} = \begin{bmatrix} \rho\hat{W} \\ \rho u\hat{W} + \hat{\xi}_x p \\ \rho v\hat{W} + \hat{\xi}_y p \\ \rho w\hat{W} + \hat{\xi}_z p \\ (\rho E + p)\hat{W} - \hat{\xi}_t p \end{bmatrix} \quad (4)$$

where

$$\hat{U} = \hat{\xi}_t + \hat{\xi}_x u + \hat{\xi}_y v + \hat{\xi}_z w \quad (5)$$

$$\hat{V} = \hat{\eta}_t + \hat{\eta}_x u + \hat{\eta}_y v + \hat{\eta}_z w \quad (6)$$

$$\hat{W} = \hat{\zeta}_t + \hat{\zeta}_x u + \hat{\zeta}_y v + \hat{\zeta}_z w \quad (7)$$

$$E = \frac{T}{\gamma(\gamma - 1)M_\infty^2} + \frac{1}{2}(u^2 + v^2 + w^2) \quad (8)$$

Here, $\hat{\xi}_x = J^{-1}\partial\xi/\partial x$ with similar definitions for the other metric quantities. The viscous fluxes $\hat{F}_v$, $\hat{G}_v$, and $\hat{H}_v$ can be found, for instance, in [21]. In the preceding expressions, u, v, w are the Cartesian velocity components, ρ the density, p the pressure, and T the temperature. The perfect gas relationship $p = \rho T/\gamma M_\infty^2$ is also assumed. All flow variables have been normalized by their respective reference freestream values except for pressure which has been nondimensionalized by $\rho_\infty u_\infty^2$.

It should be noted that the preceding governing equations correspond to the original unfiltered Navier–Stokes equations and are used without change in laminar, transitional, or fully turbulent regions of the flow. Unlike the standard large-eddy simulation (LES) approach, no additional subgrid stress and heat flux terms are appended. Instead, a high-order low-pass filter operator (to be described later) is applied to the conserved dependent variables during the solution of the standard Navier–Stokes equations. This highly discriminating filter selectively damps only the evolving poorly resolved high-frequency content of the solution. This filtering regularization procedure provides an attractive alternative to the use of standard SGS models, and has been found to yield suitable results for several canonical turbulent flows [8,9] on LES level grids. A reinterpretation of this ILES approach in the context of an approximate deconvolution model [22] has been provided by Mathew et al. [23].

III. Numerical Procedure

All simulations are performed with the extensively validated high-order Navier–Stokes solver FDL3DI [24,25]. In this code, a finite difference approach is employed to discretize the governing equations, and all spatial derivatives are obtained with high-order compact-differencing schemes [26]. For any scalar quantity ϕ, such as a metric, flux component, or flow variable, the spatial derivative ϕ' is obtained along a coordinate line in the transformed plane by solving the tridiagonal system:

$$\alpha\phi'_{i-1} + \phi'_i + \alpha\phi'_{i+1} = \beta\frac{\phi_{i+2} - \phi_{i-2}}{4} + \gamma\frac{\phi_{i+1} - \phi_{i-1}}{2} \quad (9)$$

where α, γ, and β determine the spatial properties of the algorithm. For the airfoil computations reported in this paper, a sixth-order scheme is used corresponding to $\alpha = \frac{1}{3}$, $\gamma = \frac{14}{9}$, and $\beta = \frac{1}{9}$. At boundary points, higher-order, one-sided formulas are used which retain the tridiagonal form of the scheme [24,25]. Typically, Neumann boundary conditions are implemented with third-order, one-sided expressions.

The derivatives of the inviscid fluxes are obtained by forming the fluxes at the nodes and differentiating each component with the

preceding formula. Viscous terms are obtained by first computing the derivatives of the primitive variables. The components of the viscous flux are then constructed at each node and differentiated by a second application of the same scheme.

For the case of a maneuvering airfoil, the grid is moved in a rigid fashion using the prescribed airfoil motion. To ensure that the geometric conservation law is satisfied, the time metric terms are evaluated employing the procedures described in detail in [27].

To eliminate spurious components, a high-order low-pass spatial filtering technique [24,28] is incorporated. If a typical component of the solution vector is denoted by ϕ, filtered values $\hat{\phi}$ at interior points in transformed space satisfy

$$\alpha_f\hat{\phi}_{i-1} + \hat{\phi}_i + \alpha_f\hat{\phi}_{i+1} = \Sigma_{n=0}^{N}\frac{a_n}{2}(\phi_{i+n} + \phi_{i-n}) \qquad (10)$$

Equation (10) is based on templates proposed in [26,29] and, with proper choice of coefficients, provides a $2N$th-order formula on a $2N+1$ point stencil. The $N+1$ coefficients $a_0, a_1, \ldots, a_N$, are derived in terms of α_f using Taylor- and Fourier-series analysis. These coefficients, along with representative filter transfer functions, can be found in [25,30]. The filter is applied to the conserved variables along each transformed coordinate direction once after each time step or subiteration. For the near-boundary points, the filtering strategies described in [24,30] are used. For transitional and turbulent flows, the previous high-fidelity spatial algorithmic components provide an effective implicit LES approach in lieu of traditional SGS models, as demonstrated in [8,9]. Finally, time-marching is accomplished by incorporating an iterative, implicit approximately factored procedure [8,9].

IV. Results

A. Preliminary Considerations

Both 2-D and 3-D computations were performed for the SD7003 airfoil section shown in Fig. 1. As noted earlier, this configuration has been the subject of recent experimental and numerical investigations [3–7]. This airfoil which was originally designed for low-Reynolds-number applications has a maximum thickness of 8.5% and a maximum camber of 1.45% at $x/c = 0.35$. The original sharp trailing edge was rounded with a circular arc of radius $r/c \approx 0.0004$ to facilitate the use on an O-mesh topology.

The computational baseline grid is displayed in Fig. 1, where only every other line in the azimuthal direction and every third line in the normal direction are shown. Grid points were concentrated near the airfoil to capture the transition process. Therefore, description of the wake is limited to the region just downstream of the airfoil trailing edge ($x/c < 2.0$), and study of the far wake is not considered here. This sectional 2-D grid was then employed to construct the final three-dimensional mesh, which extended a distance $s/c = 0.2$ in the spanwise direction. This value of s was selected based on a previous study of the impact of spanwise extent on the transitional flow past the same airfoil geometry at fixed angle of attack [6]. To explore spatial resolution effects, a coarser mesh was also used, and some of the mesh parameters for both grids are summarized in Table 1. The baseline mesh, used in the majority of the simulations, should provide ample resolution at these relatively low Reynolds numbers, as demonstrated in Sec. IV.B.

Given the large size of the computational grid, ILES simulations were performed using the parallel version of the high-order FDL3DI Navier–Stokes solver [31,32]. The baseline mesh was decomposed into a set of 224 overlapped subdomains or blocks which were assigned to individual processors. A five-point interblock overlap was employed to retain high-order numerical accuracy. Because of the simple topological structure of the mesh, all overlapping planes were coincident and high-order interpolation was not required.

The boundary conditions were prescribed as follows. Along the airfoil surface, a no-slip adiabatic condition was employed in conjunction with a zero normal pressure gradient. The surface velocity components (u_s, v_s) were determined from the imposed plunging motion, namely,

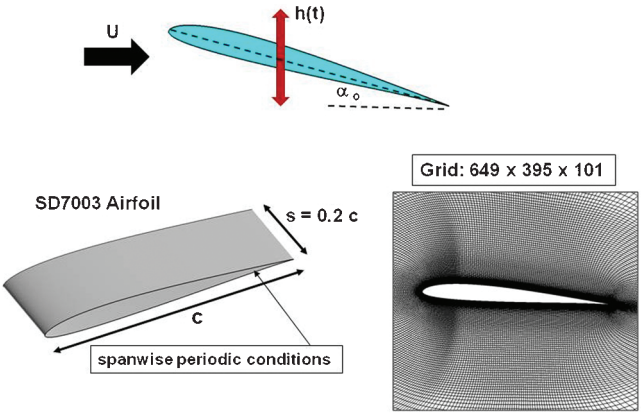

Fig. 1 Airfoil configuration and computational mesh.

$$u_s = -\dot{h}\sin\alpha_o, \qquad v_s = \dot{h}\cos\alpha_o \qquad (11)$$

$$h(t) = h_o\sin[2kF(t)t] \qquad (12)$$

$$F(t) = 1 - e^{at}, \qquad a = 4.6/t_o, \qquad t_o = 0.5 \qquad (13)$$

where α_o is the static angle of attack, h_o is the nondimensional plunging amplitude, $k = \pi fc/U_\infty$ is the reduced frequency, and $F(t)$ is a ramping function which allows for a smooth transition from a stationary airfoil to the desired periodic motion. Along the far-field boundary, located more than 100 chords away from the airfoil, freestream conditions were specified. It should be noted that, near this boundary, the grid is stretched rapidly. This stretching, in conjunction with the low-pass spatial filter, provides a buffer-type treatment found previously [33] to be quite effective in reducing spurious reflections. Spatially periodic conditions were enforced in both the azimuthal (wraparound) and spanwise (homogeneous) directions using a five-plane overlap.

Plunging simulations were started from previously computed static solutions at the corresponding mean angle of attack. Simulations were then advanced in time for typically 25 cycles to guarantee a time-asymptotic, nearly periodic state. Details of the startup process were not considered in this investigation. A very small computational nondimensional time step $\Delta tU_\infty/c = 0.00005$ was prescribed to provide sufficient temporal resolution of the abrupt spanwise breakdown of the leading-edge vortices described later on. This value of Δt corresponds to 16,000 time steps per cycle for a reduced frequency $k = 3.93$. Finally, all computations were performed employing a low freestream Mach number $M_\infty = 0.1$ with the present compressible Navier–Stokes solver. As shown later in Sec. IV.B.4, the good agreement of the computed lift coefficient with the inviscid incompressible theory demonstrated that compressibility effects were minor, at least for $k = 3.93$.

B. Results for $k = 3.93$

For the computations described in this section, the airfoil is set at a static angle of attack $\alpha_o = 4$ deg, and the reduced frequency and nondimensional plunging amplitude are $k = 3.93$ and $h_o = 0.05$, respectively. These motion parameters result in a maximum excursion in induced angle of attack of 21.5 deg which should promote unsteady leading-edge separation and the generation of

Table 1 Computational mesh parameters

Grid	size	N_U	N_L	$\Delta s_U/c$	$\Delta s_L/c$	$\Delta n/c$
Baseline	$649 \times 395 \times 101$	323	323	0.005	0.005	0.00005
Coarse	$315 \times 151 \times 101$	208	103	0.01	0.023	0.0001

[a] N_U, N_L: number of points on airfoil upper and lower surfaces
[b] $\Delta s_U/c$, $\Delta s_L/c$: maximum streamwise spacing along airfoil upper and lower surfaces
[c] $\Delta n/c$: nominal normal spacing on airfoil surface

dynamic-stall-like vortices. To explore the impact of transition on the flow structure over the plunging airfoil, three different Reynolds numbers are considered ($Re_c = 10^3,\ 10^4,\ 4 \times 10^4$). However, only the more interesting results for the two highest values of Re_c are described corresponding to recent experimental PIV measurements [7].

Both 2-D and 3-D simulations were performed to explore the suitability of the much more efficient 2-D approach for low-Reynolds-number applications, as well as to compare with previous computations [7]. A comparison of the instantaneous spanwise vorticity component obtained from both 2-D and 3-D calculations is shown at a given phase of the plunging motion in Fig. 2. For $Re_c = 10^4$ (Figs. 2a and 2b), the 2-D and 3-D results are found to be in close agreement with each other over a significant portion of the airfoil. The leading-edge vortex formation, in particular, exhibits a well-defined and persistent two-dimensional character. Some minor discrepancies exist in the aft portion near the trailing edge, as well as in the near wake due to incipient transitional effects. Therefore, for the given plunging parameters and $Re_c = 10^4$, the flow structure is effectively laminar, and predictable to a great extent by the two-dimensional computational approach. As the Reynolds number is increased to 4×10^4, significant differences emerge between 2-D and 3-D results (Figs. 2c and 2d). The coherent vortices observed in the 2-D simulations break down in the spanwise direction, in a process to be described in more detail later. Given the importance of spanwise effects, emphasis will be placed on the 3-D computations in the following sections.

A limited assessment of mesh resolution was performed using the two computational grids described earlier. Figure 3 shows the effect of spatial resolution on the computed phase-averaged spanwise vorticity for both values of Reynolds number at a selected phase of the plunging cycle. Results on the baseline and coarse meshes display the same overall flow structure above the airfoil, despite the significant differences in grid spacing. However, the coherent flow features exhibit a sharper character on the finer (baseline) mesh. Further evidence of adequate mesh resolution is provided later in Sec. IV.B.4 when comparing the computed mean drag coefficients.

1. *Flowfield Structure for $Re_c = 10^4$*

The instantaneous and phase-averaged computed flow structures over the plunging airfoil for $Re_c = 10^4$ are shown in Fig. 4. Following the designation of McGowan et al. [7], the selected phases correspond to the positions of maximum upward displacement ($\Phi = 0$), maximum downward velocity ($\Phi = \frac{1}{4}$), maximum downward displacement ($\Phi = \frac{1}{2}$), and maximum upward velocity ($\Phi = \frac{3}{4}$). The instantaneous flow is plotted on the midspan plane. The computed phase-averaged flow was obtained by first averaging in the spanwise homogeneous direction and then over 7 cycles of the motion. The overall instantaneous and phase-averaged flow structures are found to be in reasonable agreement with each other. This demonstrates the limited impact of spanwise effects, as well as the effectively periodic nature of this low-Reynolds-number forced flow. Some minor differences exist in the vortex braids in the near wake, as well as in the

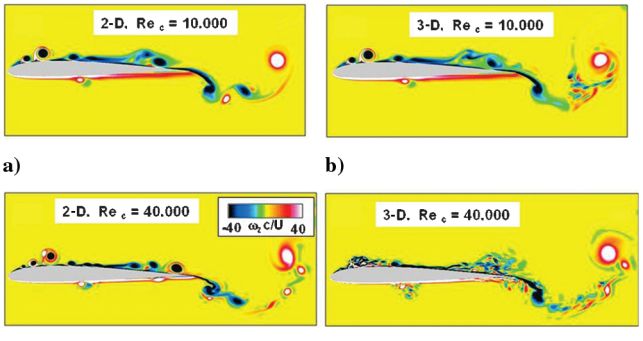

Fig. 2 Comparison of instantaneous spanwise vorticity for 2-D and 3-D simulations, $k = 3.93$, $\alpha_o = 4°$.

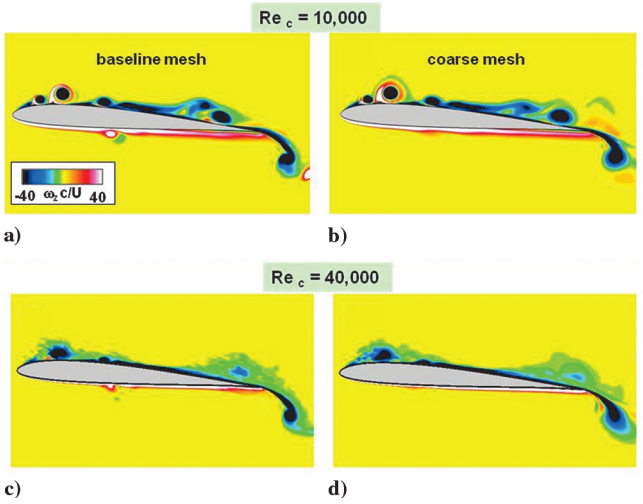

Fig. 3 Effect of grid resolution on computed phase-averaged vorticity, $k = 3.93$, $\alpha_o = 4°$.

secondary vorticity which is ejected from the airfoil upper surface due to the strong vortex–surface interaction. Because of the large angle of attack induced by the plunging motion during the downstroke, leading-edge separation occurs on the upper surface of the airfoil, and coherent dynamic-stall-like vortices are generated. Two distinct leading-edge vortices (denoted as numbers 1 and 2 in Fig. 4c) are formed by the time the airfoil reaches its bottom dead center. During the upstroke, these vortices propagate close to the airfoil surface, thereby precluding massive stall for this high value of reduced frequency. Given the short period of the motion ($T = \pi/k = 0.8$), the dynamic-stall vortices emerge before the pair of vortices generated in the previous cycle (denoted as numbers 3 and 4 in Fig. 4d) have reached the airfoil trailing edge. In addition to the primary leading-edge vortical structures, another distinct feature is the ejection of

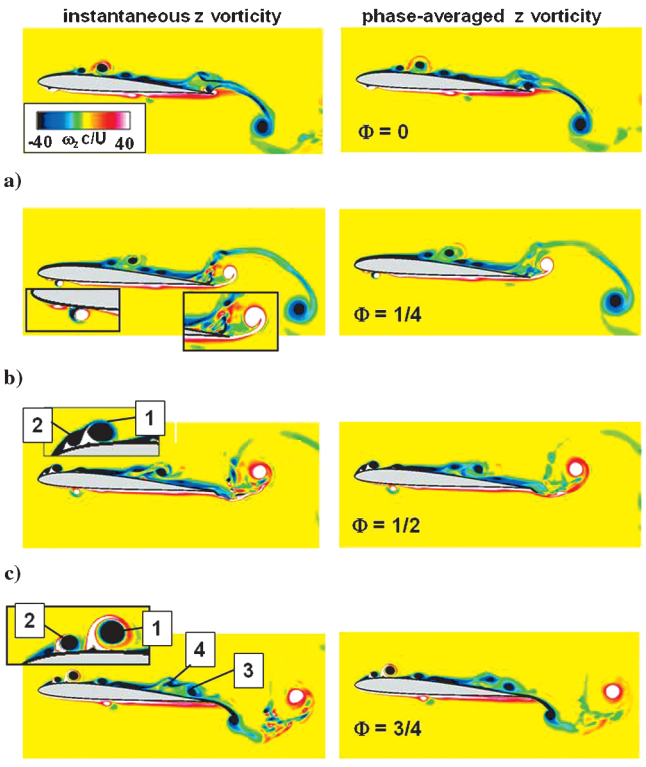

Fig. 4 Comparison of instantaneous (left) and phase-averaged (right) spanwise vorticity at selected phases of the plunging motion, $k = 3.93$, $\alpha_o = 4°$, $Re_c = 10^4$.

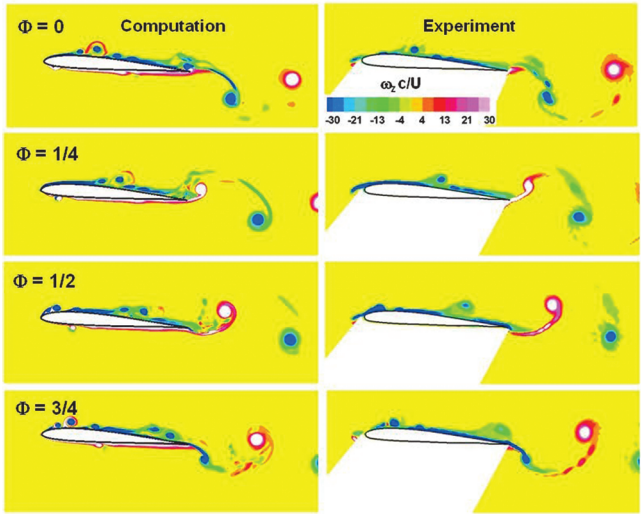

Fig. 5 Comparison of computed (left) and experimental (right) phase-averaged spanwise vorticity at selected phases of the plunging motion, $k = 3.93$, $\alpha_o = 4°$, $Re_c = 10^4$.

vorticity of the opposite sign due to the ensuing vortex–surface interaction. This ejected vorticity is quite prominent between the two primary dynamic-stall vortices (Fig. 4d), and eventually completely surrounds the leading vortex (denoted as 1). Further downstream, this secondary vorticity becomes less apparent due to spanwise instability effects, as discussed later. Separation and formation of a single dynamic-stall vortex is also observed on the airfoil lower surface (Fig. 4b) as a result of the large negative angle of attack induced during the upstroke. The dynamic-stall vortices generated near the airfoil leading edge on the upper and lower surface of the airfoil are observed to be more prominent at the end of the downstroke and upstroke, respectively (Figs. 4a and 4c), rather than at the phases of maximum downward or upward velocity. This lack of correlation with instantaneous induced angle of attack is in part due to the well-known separation delay associated with the phenomenon of dynamic stall, wherein vortices emerge following an unsteady boundary-layer separation process over the rounded leading edge. This behavior contrasts with the vortices generated by the sharp trailing edge of the plunging airfoil. As seen in Figs. 4b and 4d, the formation of the trailing-edge vortices is found to be more correlated with the phases of maximum plunging velocity.

A comparison of the computed and experimental phase-averaged vortical structures is displayed in Fig. 5. Good overall agreement is observed in terms of the coherent vortical structures, although the computed results exhibit better defined flow features over the airfoil. It should be noted that the experiments are averaged over many more cycles, which becomes prohibitive in the present 3-D calculations. The experimental PIV resolution is limited by the desire to achieve a global measurement including the wake. Also, details of the flow below the airfoil are not provided in the experiments due to optical access constraints.

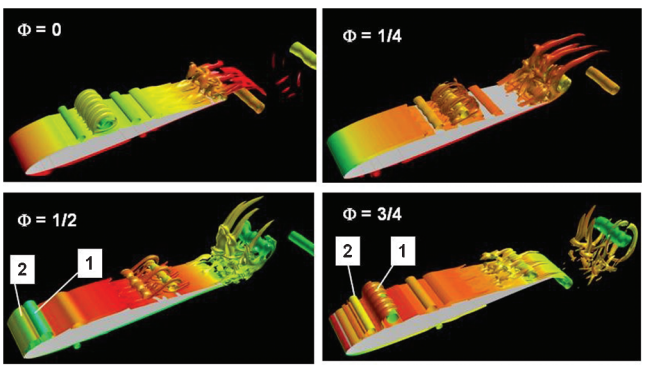

Fig. 6 Isosurfaces of instantaneous vorticity magnitude, $k = 3.93$, $\alpha_o = 4°$, $Re_c = 10^4$.

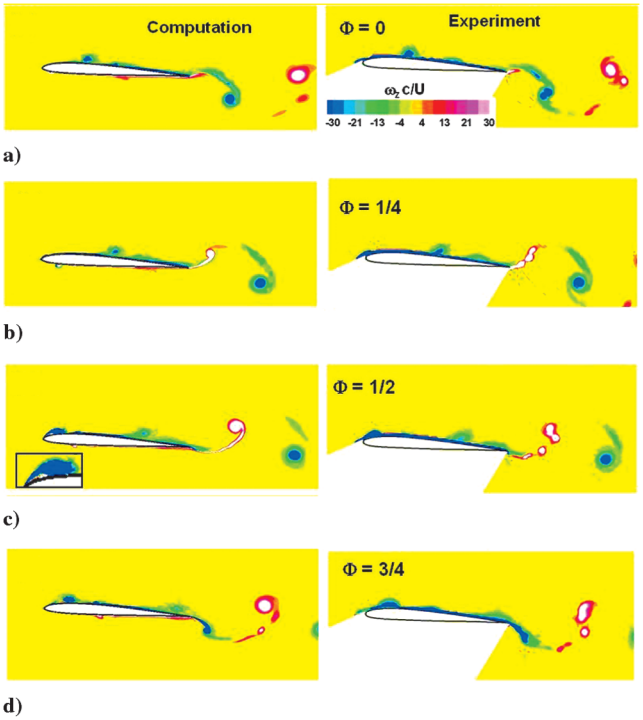

Fig. 7 Comparison of computed (left) and experimental (right) phase-averaged spanwise vorticity at selected phases of the plunging motion, $k = 3.93$, $\alpha_o = 4°$, $Re_c = 4 \times 10^4$.

The present implicit large-eddy simulations permit a detailed description of the three-dimensional instantaneous flow structure which complements experimental planar observations. The overall instantaneous 3-D flow features are displayed for several phases in Fig. 6. These plots show an isosurface of vorticity magnitude colored by density to enhance contrast. At all phases of the plunging motion shown, one can observe coherent spanwise vortical structures or rollers that exhibit a fairly two-dimensional character. These vortices are surrounded by complex three-dimensional flow features resulting from spanwise instabilities. In particular, the dynamic-stall vortex system forming near the leading edge retains its spanwise coherence. However, the vorticity ejected from the airfoil surface (due to the strong vortex–surface interaction) rapidly breaks down, giving rise to the appearance of longitudinal vortical structures. In the near wake, the primary vortices shed from the plunging trailing edge exhibit a two-dimensional character, whereas the feeding sheets associated with these vortices break down into fine-scale structures. It is quite likely that the primary wake vortices will also exhibit spanwise

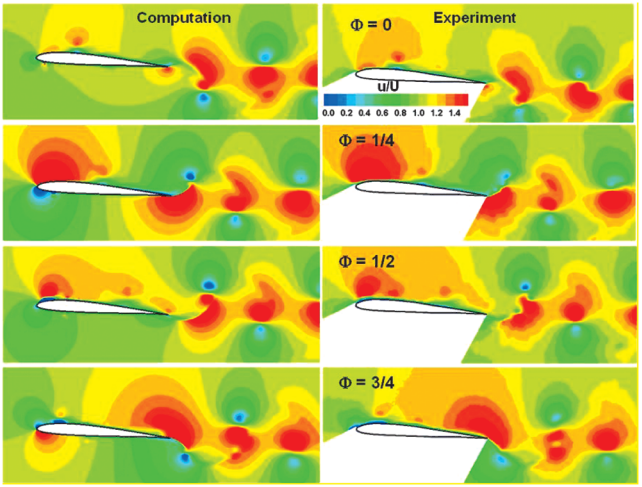

Fig. 8 Comparison of computed (left) and experimental (right) phase-averaged streamwise velocity at selected phases of the plunging motion, $k = 3.93$, $\alpha_o = 4°$, $Re_c = 4 \times 10^4$.

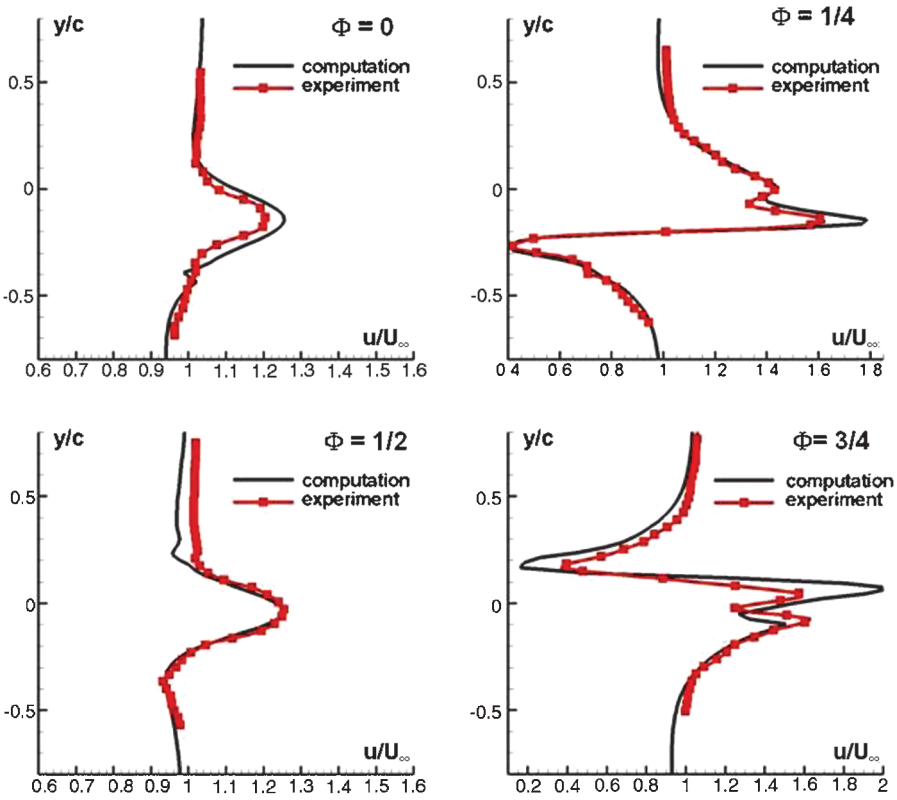

Fig. 9 Comparison of computed and experimental streamwise velocity profiles in the near wake ($x/c = 1.5$), $k = 3.93$, $\alpha_o = 4°$, $Re_c = 4 \times 10^4$.

instabilities further downstream of the airfoil. However, investigating this behavior is outside the scope of the present work and would require a much finer and wider computational mesh in the far wake region. In summary, for this high reduced frequency and low Reynolds number, transitional effects over the airfoil appear to be minor and are associated with the secondary vortical structures and with the vortex sheets feeding the coherent primary vortices. As discussed next, this situation changes significantly with increasing Reynolds number.

2. *Flowfield Structure for $Re_c = 4 \times 10^4$*

In this section, the global flow structure around the plunging airfoil is first examined and compared with experiment, followed by a more detailed description of the dynamic-stall vortex formation and transition near the leading edge. The computed phase-averaged flow structure for this higher Reynolds number is displayed in Figs. 7–9 in terms of the streamwise velocity component and the spanwise vorticity. These figures also display the corresponding experimental measurements of [7]. The computed and experimental phase-averaged velocity fields are observed to be in good agreement with each other over the entire domain shown in Fig. 8. A more detailed comparison of velocity profiles in the near wake at $x/c = 1.5$ is provided in Fig. 9. The agreement between the measured and computed profiles is, in general, quite good. The velocity profiles corresponding to the phases of maximum vertical displacement ($\Phi = 0, \frac{1}{2}$) exhibit a well-defined jet character. This jetlike behavior is consistent with the fact that the trailing-edge vortex shed from the airfoil lower surface is above the vortex shed from the upper surface boundary layer (see Figs. 7a and 7c). As will be shown in Sec. IV.B.4, this inverted vortex street results in a net mean thrust (rather than drag) on the plunging airfoil.

Increasing the Reynolds number has clearly modified the details of the phase-averaged vortical structure emerging from the unsteady separation process near the airfoil leading edge. As discussed earlier for $Re_c = 10^4$ (Fig. 4c), the leading-edge vortex system exhibited a pair of dynamic-stall-like vortices which retained their identity as they propagated downstream in the absence of significant spanwise transitional effects. By contrast, for $Re_c = 4 \times 10^4$ (Fig. 7c), a single and more diffused leading-edge vortex is observed in the phase-averaged representation. This dynamic-stall vortex has dissipated significantly by the time it approaches the airfoil trailing edge (Fig. 7d).

A comparison of the computed instantaneous and phase-averaged spanwise vorticity fields is shown in Fig. 10. Significant differences are observed between the instantaneous and phase-averaged representations which reflect the fully three-dimensional transitional nature of the flow. The instantaneous vorticity exhibits fine-scale flow features within the dynamic-stall vortices, as well as in the near wake. These features are essentially eliminated in the phase-averaging process.

The computed instantaneous three-dimensional flow structures below and above the plunging airfoil are displayed in Figs. 11 and 12, respectively. Underneath the airfoil (Fig. 11), one can observe the

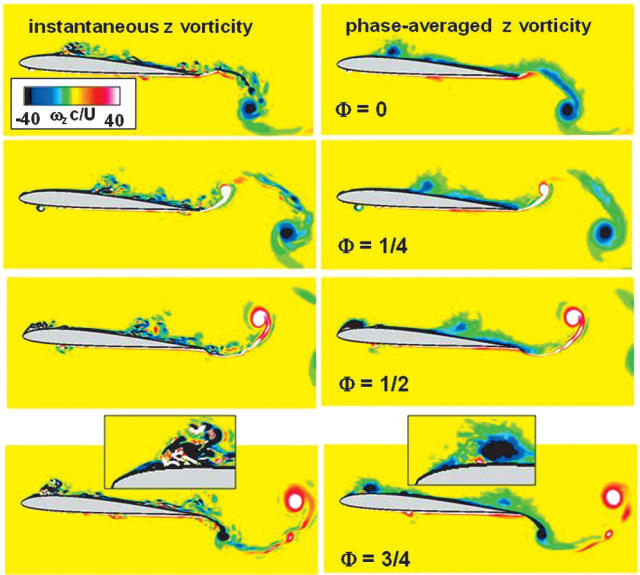

Fig. 10 Comparison of computed instantaneous (left) and phase-averaged (right) spanwise vorticity at selected phases of the plunging motion, $k = 3.93$, $\alpha_o = 4°$, $Re_c = 4 \times 10^4$.

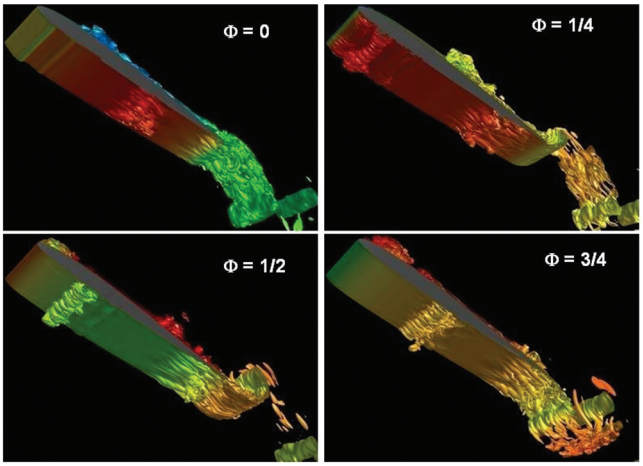

Fig. 11 Isosurfaces of instantaneous vorticity magnitude showing three-dimensional flow structure underneath plunging airfoil, $k = 3.93$, $\alpha_o = 4°$, $Re_c = 4 \times 10^4$.

formation and propagation of a leading-edge vortex that is generated during the upstroke by the motion-induced negative angle of attack. The flow exhibits transitional features associated with the ejection of wall vorticity as the vortex interacts with the surface. A much more complex instantaneous flow structure can be observed above the airfoil (Fig. 12). The most prominent overall flow features are the leading-edge vortices and their breakdown into fine-scale turbulence due to spanwise instability effects. At the position of maximum upward displacement ($\Phi = 0$), the boundary layer near the leading edge remains laminar and attached to the airfoil surface. By the time the airfoil has reached its maximum downward velocity ($\Phi = \frac{1}{4}$), an incipient region of laminar separation has emerged near the leading edge. Between $\Phi = \frac{1}{4}$ and $\Phi = \frac{1}{2}$, this separation region evolves into a coherent dynamic-stall-like vortex, which subsequently breakdowns into fine-scale structures. This transitional leading-edge vortex propagates downstream close to the airfoil surface, as seen in Fig. 10. Again, given the relatively high value of reduced frequency, the dynamic-stall-like vortex generated in the previous cycle (denoted as V_1 in Fig. 12c) has not reached the airfoil trailing edge before a new leading-edge vortex V_2 is generated.

The mixed laminar–transitional character of this highly unsteady flow is quite apparent. For instance, the vortex structure of Fig. 12c displays an extensive region of fairly laminar flow between the two transitional leading-edge vortices generated in consecutive cycles of the plunging motion. This mixed flow structure, although amenable to simulation with the present high-fidelity ILES approach, will remain a significant challenge for more efficient Reynolds-averaged methods incorporating simplified transition models.

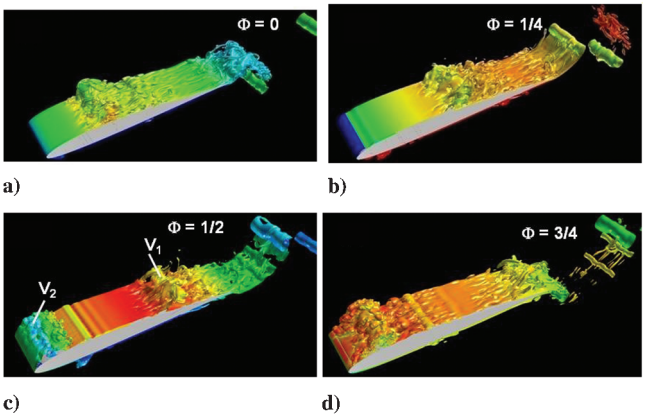

Fig. 12 Isosurfaces of instantaneous vorticity magnitude showing three-dimensional flow structure above plunging airfoil, $k = 3.93$, $\alpha_o = 4°$, $Re_c = 4 \times 10^4$.

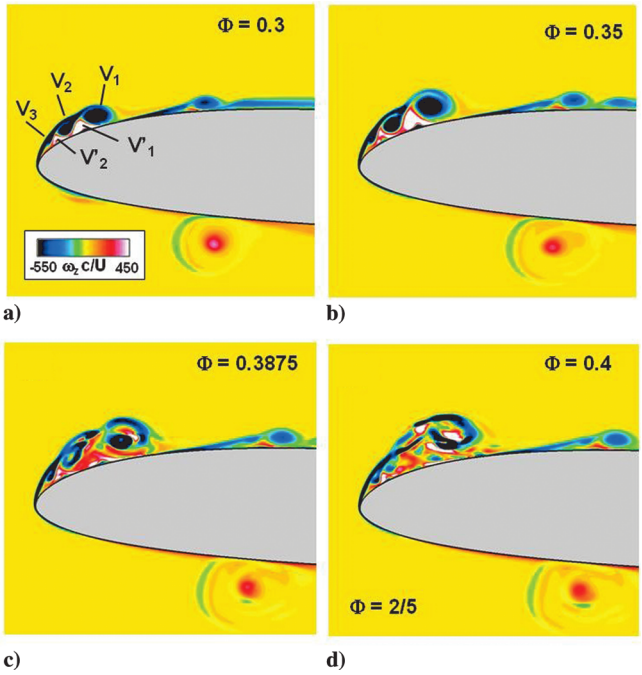

Fig. 13 Instantaneous spanwise vorticity near the leading edge during the onset of transition in the dynamic-stall vortex system, $k = 3.93$, $\alpha_o = 4°$, $Re_c = 4 \times 10^4$.

3. Transition of Dynamic-Stall Vortex

The process of transition of the leading-edge vortex system for $Re_c = 4.0 \times 10^4$ is examined in more detail in this section. The instantaneous vortical flow structure near the leading edge is shown in Fig. 13 at several instants during the onset of transition. The corresponding near-wall structure is also displayed in Fig. 14 which shows contours of the spanwise vorticity component on a plane parallel to the airfoil surface at a normal distance of approximately $\Delta n/c = 0.002$. At $\Phi = 0.3$ (Fig. 14a), the flowfield near the leading edge exhibits a two-dimensional character with insignificant spanwise variations. At this time, following separation, a dynamic-stall vortex system has already emerged (Fig. 13a) and comprises three primary (clockwise) vortices (denoted as V_1, V_2, V_3), as well as two distinguishable secondary (counterclockwise) vortical structures (denoted as V_1', V_2'). There are additional incipient tertiary structures adjacent to the surface that cannot be discerned in the scale of the figure. By $\Phi = 0.35$, these vortices have increased in size while still retaining their coherent structure (Fig. 13b). However, spanwise

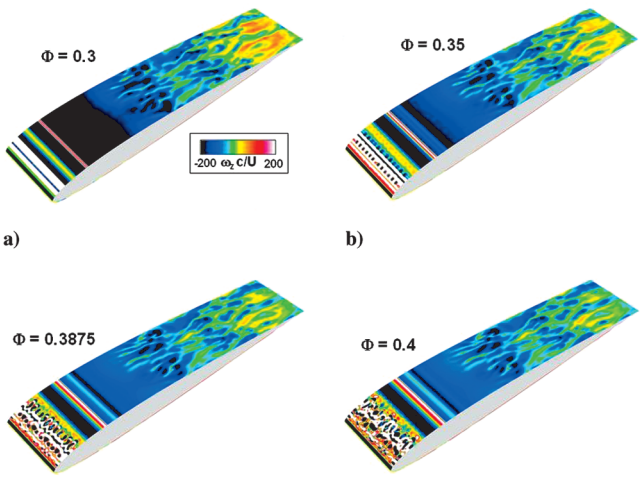

Fig. 14 Instantaneous spanwise vorticity near the airfoil surface during the onset of transition, $k = 3.93$, $\alpha_o = 4°$, $Re_c = 4 \times 10^4$.

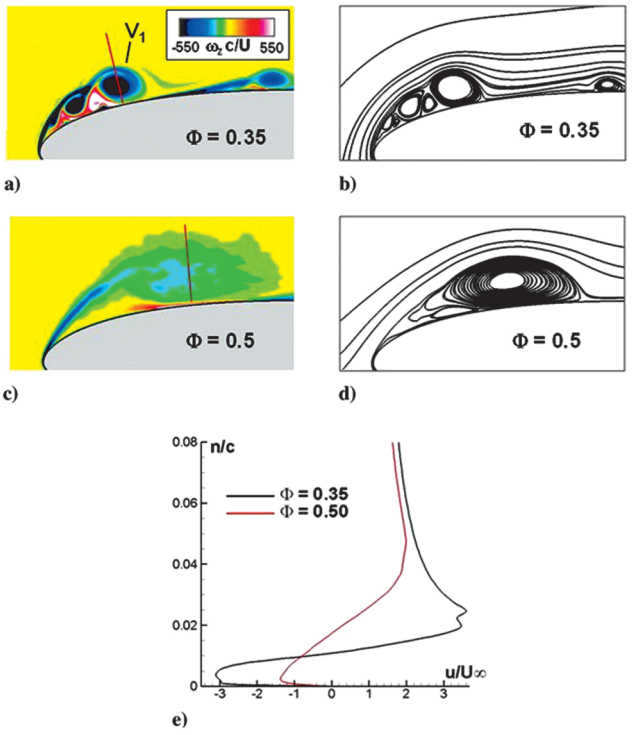

Fig. 15 Phased-averaged dynamic-stall vortex structure before and after the onset of transition: (a,c) spanwise vorticity, (b,d) streamline topology in the airfoil frame of reference, and (e) streamwise velocity profiles through the center of the vortex ($k = 3.93$, $\alpha_o = 4°$, $Re_c = 4 \times 10^4$).

instabilities have just emerged, as shown in the corresponding near-surface plot of Fig. 14b. Between $\Phi = 0.35$ and $\Phi = 0.3875$, the dramatic breakdown of the leading-edge vortex system is apparent, as seen in Figs. 13c and 14c. The outline of the original concentrations of vorticity in the laminar dynamic-stall vortex system are still discernible in Fig. 13c, however, by $\Phi = 0.4$, the flow structure has evolved into a single transitional leading-edge vortex. Another qualitative change in flow structure associated with the premature breakdown of the dynamic-stall vortices is the elimination of the regular secondary vorticity ejection process noted earlier at lower Reynolds number (seen in Fig. 4d).

The transformation of the phase-averaged leading-edge vortex structure following the onset of transition is also examined in more detail, because this type of representation is commonly rendered in experimental studies. Before breakdown, while the flow is effectively laminar, the dynamic-stall vortices are very compact and characterized by fairly high values of vorticity magnitude (Fig. 15a). By the time the spanwise breakdown is essentially completed, a rather diffused vortex remains (Fig. 15c) with maximum values of vorticity in its core that are an order of magnitude smaller than those existing initially within vortex V_1 in Fig. 15a. This significant reduction in phase-averaged vorticity is not solely the result of viscous dissipation but rather it is promoted by the cancellation of primary (negative) vorticity with the secondary (positive) vorticity ejected from the wall (as seen in the instantaneous representation, Fig. 13d). The corresponding phase-averaged streamwise velocity profiles through the center of the vortex are shown in Fig. 15e. Following transition, the reversed-flow velocity magnitude decreases drastically, with a similar pronounced reduction of the maximum velocity overshoot. Finally, the streamline topology in the frame of reference moving with the airfoil is displayed in Figs. 15b and 15d. The laminar dynamic-stall vortex system comprises multiple vortices (or foci), as previously observed in 2-D simulations [15,16]. Following transition, a simpler topological pattern emerges characterized by a larger clockwise vortex, as well as by a near-wall counterclockwise structure.

The spanwise breakdown of the laminar dynamic-stall vortex previously described is clearly abrupt and takes place over a non-dimensional time interval of order $\Delta t U_\infty / c \leq 0.04$. This represents a fast onset relative to either the plunging motion or the vortex convection time scales. It remains to be seen whether this process can be duplicated by standard Reynolds-averaged eddy-viscosity models

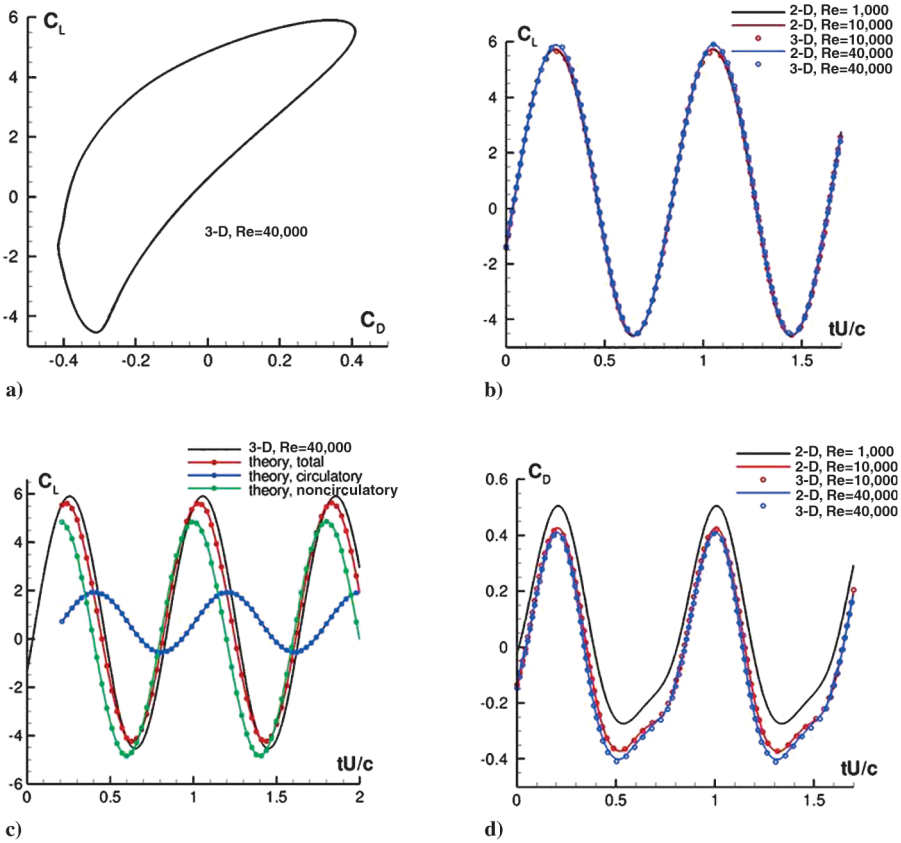

Fig. 16 Computed lift and drag coefficient histories, $k = 3.93$, $\alpha_o = 4°$.

Table 2 Computed mean drag coefficient for $k = 3.93$ cases

Re_c	Grid	$C_{D_{\text{mean}}}$
10^3	2-D, baseline	0.049
10^4	2-D, baseline	−0.056
10^4	2-D, coarse	−0.053
10^4	3-D, baseline	−0.055
4×10^4	2-D, baseline	−0.076
4×10^4	3-D, baseline	−0.083
4×10^4	3-D, coarse	−0.082

that rely on dissipationlike terms. In addition, high-resolution experimental measurements concentrated on the leading-edge vortex formation and transition are currently lacking.

4. Aerodynamic Loads

The lift and drag coefficient histories for several of the computed cases are shown in Fig. 16. A typical plot of C_L and C_D for three consecutive cycles of the plunging motion (Fig. 16a) demonstrates the fairly periodic nature of the aerodynamic loads. The time histories of the lift coefficient for several Reynolds numbers, as well as for both 2-D and 3-D calculations are shown in Fig. 16b. Clearly, C_L appears to be essentially independent of Reynolds number and of the three-dimensional transitional aspects of the flowfield. The insensitivity of the aerodynamic lift is due to the fact that, at this high value of reduced frequency, C_L is dominated by the acceleration of the airfoil which scales with k^2. Indeed, the computed lift is found to be in close agreement with the prediction given by the inviscid theory [34] (Fig. 16c) which in turn is shown to be dominated by noncirculatory effects.

Several of the computed drag coefficient histories are displayed in Fig. 16d, and the mean values of C_D are summarized in Table 2. Positive mean C_D values correspond to drag, whereas negative values imply net thrust on the airfoil. As it is perhaps to be expected, the drag coefficient shows significant dependence on Reynolds number. With the exception of the results for $Re_c = 10^3$, the plunging airfoil experiences a mean net thrust which increases with Reynolds number. For $Re_c = 10^4$, the computed 2-D and 3-D thrust (on the baseline mesh) are in close agreement with each other, consistent with the limited transitional effects. For $Re_c = 4 \times 10^4$, differences emerge between 2-D and 3-D computations due to the transitional nature of the flowfield. Finally, it should also be noted that, for both Reynolds numbers, the effects of spatial resolution on the mean drag coefficient are found to be minor, demonstrating a measure of grid independence.

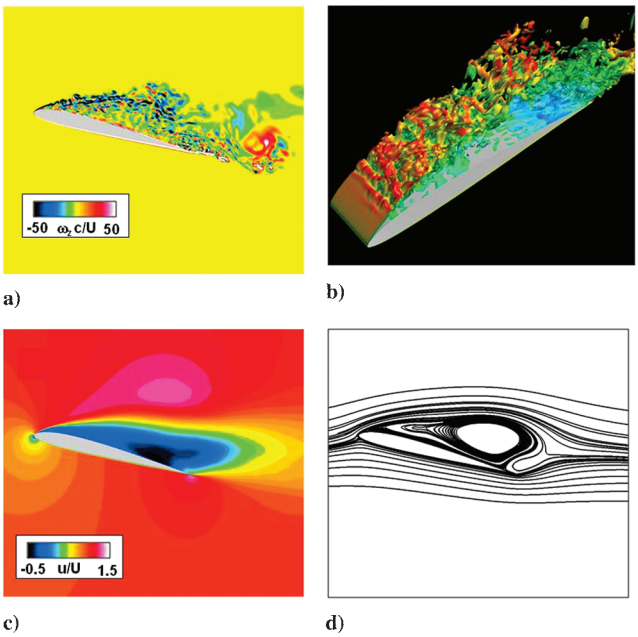

Fig. 17 Unsteady and time-averaged flow structure for static conditions, $\alpha_o = 14°$, $Re_c = 6 \times 10^4$. (a) instantaneous spanwise vorticity, (b) isosurface of instantaneous vorticity magnitude, (c) time-averaged streamwise velocity, and (d) mean streamline pattern.

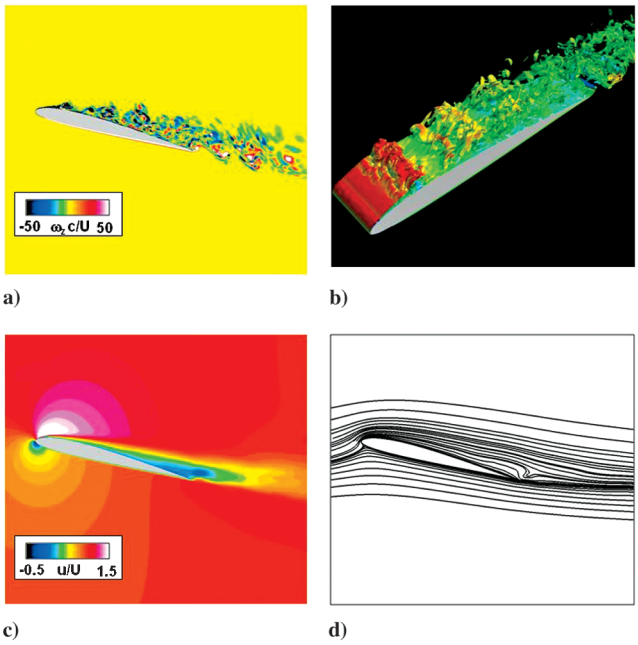

Fig. 18 Unsteady and time-averaged flow structure for high-frequency, small-amplitude plunging conditions, $\alpha_o = 14°$, $Re_c = 6 \times 10^4$, $k = 10$ and $h_o = 0.005$. (a) instantaneous spanwise vorticity, (b) isosurface of instantaneous vorticity magnitude, (c) time-averaged streamwise velocity, and (d) mean streamline pattern.

C. Stall Suppression Using High-Frequency, Small-Amplitude Oscillations

In this section, the impact of high-frequency small-amplitude plunging oscillations on the stalled flow past the airfoil is considered. The static angle of attack is set at $\alpha_o = 14$ deg, which corresponds to the poststall regime for the stationary airfoil. The prescribed reduced frequency is $k = 10$ and the nondimensional plunging amplitude varied from $h_o = 0.005$ to $h_o = 0.04$. The corresponding maximum excursion in angle of attack induced by the motion ranged from 5.7 to 38.6 deg. Two different values of Reynolds number ($Re_c = 10^4$ and 6×10^4) are considered to explore transition effects.

The instantaneous and time-averaged flow structures for the stationary airfoil at $Re_c = 6 \times 10^4$ are displayed in Fig. 17. At this angle of attack, the baseline flow is fully stalled and is characterized in the mean by a large recirculation region above the airfoil (Figs. 17c and 17d). The instantaneous plot in Fig. 17a shows the shedding of large-scale vortices generated from the separated shear layers at the leading and trailing edges. At this higher Reynolds number, the flow is clearly transitional, and both the shear layer and shed vortices exhibit fine-scale features.

The impact on the flowfield of the imposed high-frequency, small-amplitude plunging oscillations (with $h_o = 0.005$) is shown in Fig. 18. As a consequence of the airfoil vibrations, the time-averaged flow becomes fully attached (Fig. 18d), and acceleration around the leading edge is clearly observed in the mean streamwise velocity contours (Fig. 18c). The instantaneous flow structure (Fig. 18a) shows the formation of coherent dynamic-stall-like vortices which are generated near the leading edge due to the large motion-induced

Table 3 Computed mean drag coefficient for $k = 10$ cases

Re_c	$h_o = 0.0$	$h_o = 0.005$	$h_o = 0.025$	$h_o = 0.04$
10^4	0.251	0.162	0.036	−0.254
6×10^4	0.225	0.133	-	-

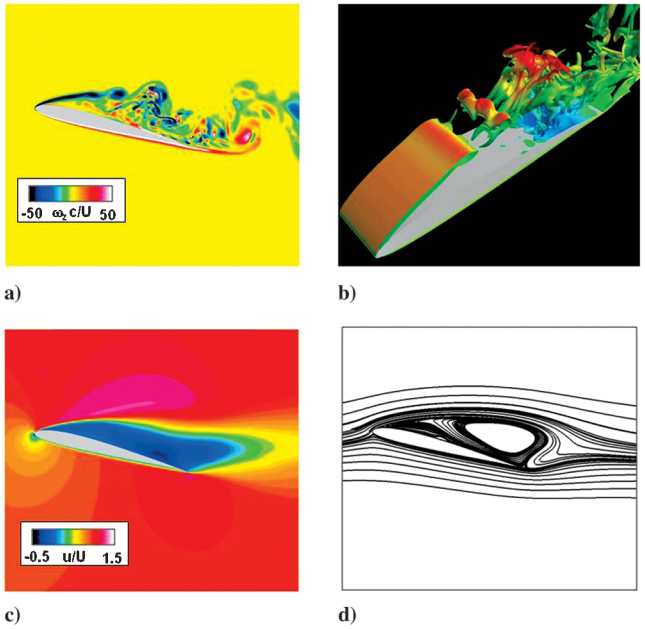

Fig. 19 Unsteady and time-averaged flow structure for static conditions, $\alpha_o = 14°$, $Re_c = 10^4$. (a) instantaneous spanwise vorticity, (b) isosurface of instantaneous vorticity magnitude, (c) time-averaged streamwise velocity, and (d) mean streamline pattern.

angle of attack. These vortices propagate close to the airfoil surface and quickly breakdown as a consequence of spanwise instabilities (Fig. 18b). The effect of the forcing on the computed mean drag coefficient is given in Table 3 which indicates that an approximately 40% reduction in C_D (relative to the static case) is achieved with the very small-amplitude plunging motion.

High-frequency forcing is therefore found to be very effective in eliminating the mean separation, and this situation is, in this regard, similar to previous flow control work employing synthetic jets [35] and plasma-type actuators [36]. Although it was not accomplished in this research, it would be of interest to consider the effect of even smaller oscillation amplitude for the purpose of further exploring

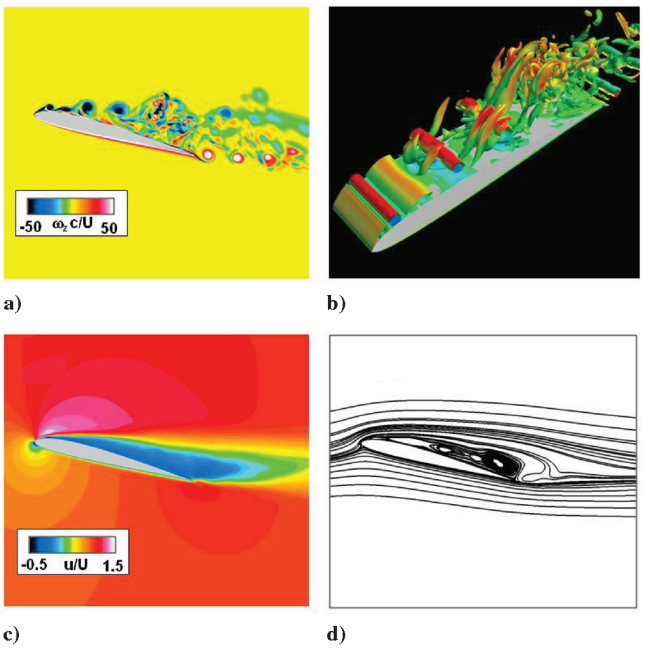

Fig. 20 Unsteady and time-averaged flow structure for high-frequency, small-amplitude plunging conditions, $\alpha_o = 14°$, $Re_c = 10^4$, $k = 10$ and $h_o = 0.005$. (a) instantaneous spanwise vorticity, (b) isosurface of instantaneous vorticity magnitude, (c) time-averaged streamwise velocity, and (d) mean streamline pattern.

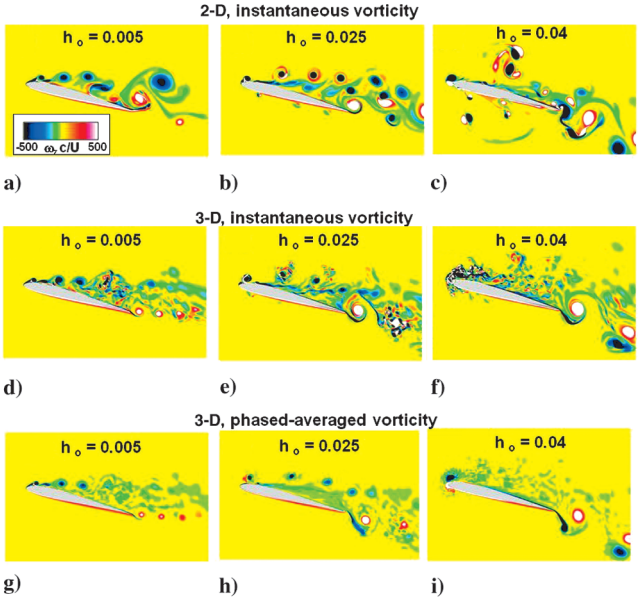

Fig. 21 Effect of plunging amplitude on stall suppression, $\alpha_o = 14°$, $Re_c = 10^4$, $k = 10$.

control effectiveness. Nonetheless, the present results clearly demonstrate that these low-Reynolds-number flows are quite receptive to either prescribed or unintended vibrations. This property could potentially be exploited in small and micro air vehicles through either suitable actuation or aeroelastic tailoring.

To investigate if the previously observed control effectiveness extends to lower Reynolds numbers, a similar situation was considered for $Re_c = 10^4$. The baseline stationary flow is shown in Fig. 19 in terms of its instantaneous and time-averaged structures. The flow over the airfoil is again fully stalled and displays a large recirculation region. The shear layer separating from the leading edge rolls up into coherent vortices (Figs. 19a and 19b) which exhibit less transitional fine-scale features relative to the higher Reynolds number case.

The change of the flow structure following the application of high-frequency plunging oscillations with $h_o = 0.005$ is shown in Fig. 20. Comparison of the mean flow structure with the baseline case demonstrates that a reduction in the size of the recirculation zone is still possible. However, the effectiveness of the forcing has diminished relative to the higher Reynolds number counterpart. Because of the imposed airfoil motion, dynamic-stall vortices are generated periodically near the leading edge and convect over the airfoil surface (Figs. 20a and 20b). These vortices remain fairly coherent and two-dimensional over a significant portion of the

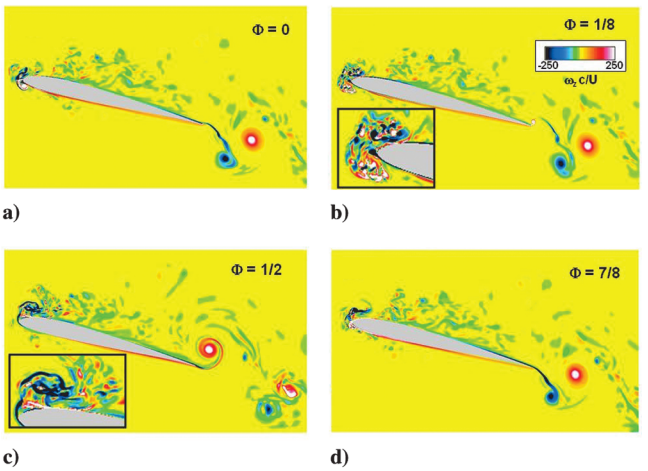

Fig. 22 Instantaneous spanwise vorticity for high-frequency, small-amplitude plunging, $\alpha_o = 14°$, $Re_c = 10^4$, $k = 10$ and $h_o = 0.04$.

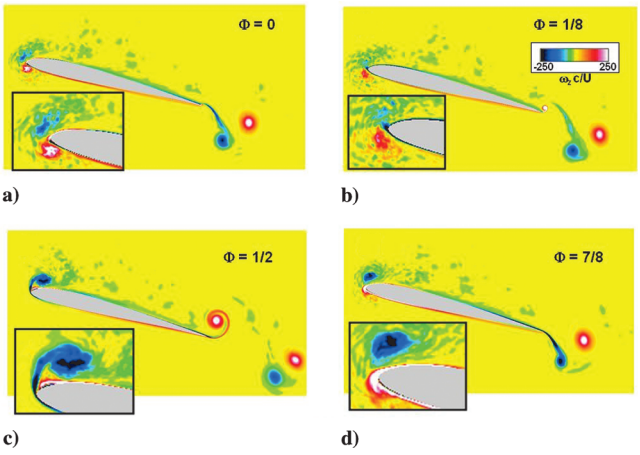

Fig. 23 Phased-averaged spanwise vorticity for high-frequency, small-amplitude plunging, $\alpha_o = 14°$, $Re_c = 10^4$, $k = 10$ and $h_o = 0.04$.

airfoil. Spanwise transitional effects eventually emerge in the aft-portion of the airfoil. However, the breakdown into fine-scale features is not as pronounced as previously noted for $Re_c = 6 \times 10^4$ (Fig. 18).

To further improve stall suppression effectiveness at the lower Reynolds number, an increase in the plunging amplitude was considered. Both 2-D and 3-D computations were performed for the airfoil plunging with a fixed high frequency ($k = 10$) and amplitudes ranging from $h_o = 0.005$ to $h_o = 0.04$. The effect of plunging amplitude on the instantaneous flow structure is shown in the top row of Fig. 21 for the 2-D computations using spanwise vorticity contours. The corresponding instantaneous and phase-averaged plots for the full 3-D simulations are shown in the middle and bottom rows of the same figure, respectively. As a first observation, it can be noted that, even for this fairly low Reynolds number, the effects of transition cannot be ignored. This contrasts with the results for $k = 3.93$, $Re_c = 10^4$, and much smaller static angle of attack ($\alpha_o = 4$ deg) for which, as discussed earlier in Sec. IV.B.1, transitional effects were found to be minor.

For $h_o = 0.005$, the 2-D approach (Fig. 21a) correlates well with the full 3-D computations (Fig. 21d) on the front half of the airfoil. However, significant discrepancies emerge in the aft-portion of the airfoil and in the near wake.

As the plunging amplitude is increased to $h_o = 0.025$, the shed dynamic-stall vortices exhibit the onset of transitional effects much closer to the leading edge (Fig. 21e). Nonetheless, the overall flow structure is still characterized in both 2-D and 3-D simulations by the shedding of discrete leading-edge vortices which convect over the airfoil in a fairly regular fashion.

When the oscillation amplitude is increased further to $h_o = 0.04$, a dramatic transformation in the global flow structure ensues. In the 2-D simulations (Fig. 21c), a very chaotic flow emerges containing strong vortex pairs which propagate (due to their self-induced velocity) far away from the airfoil. The dynamic-stall vortex system moves in front of the leading edge, as seen in the particular instant shown in the figure. This chaotic flow structure is generated in part due to the inability of the 2-D approach to incorporate the transitional behavior of the coherent vortices. In the 3-D computations (Figs. 21f and 21i), there is also a significant change in flow structure for $h_o = 0.04$. The dynamic-stall vortex system is observed to move in front and around the airfoil leading edge, and appears to experience a full breakdown. In addition, the regular train of vortices that propagates over the airfoil at smaller plunging amplitudes is no longer observed. It should be noted that this dramatic change in qualitative flow structure has been confirmed experimentally [12] for a plunging NACA 0012 airfoil at the same Reynolds number.

The very interesting flow behavior emerging at the highest amplitude ($h_o = 0.04$) is examined in more detail in Figs. 22–25. The flow structure in the near-wake region (Figs. 22 and 23) is characterized by the regular shedding of a strong pair of (opposite sign) vortices which propagate in a strong downward direction. This contrasts with the low-amplitude case ($h_o = 0.005$, Fig. 21d) wherein

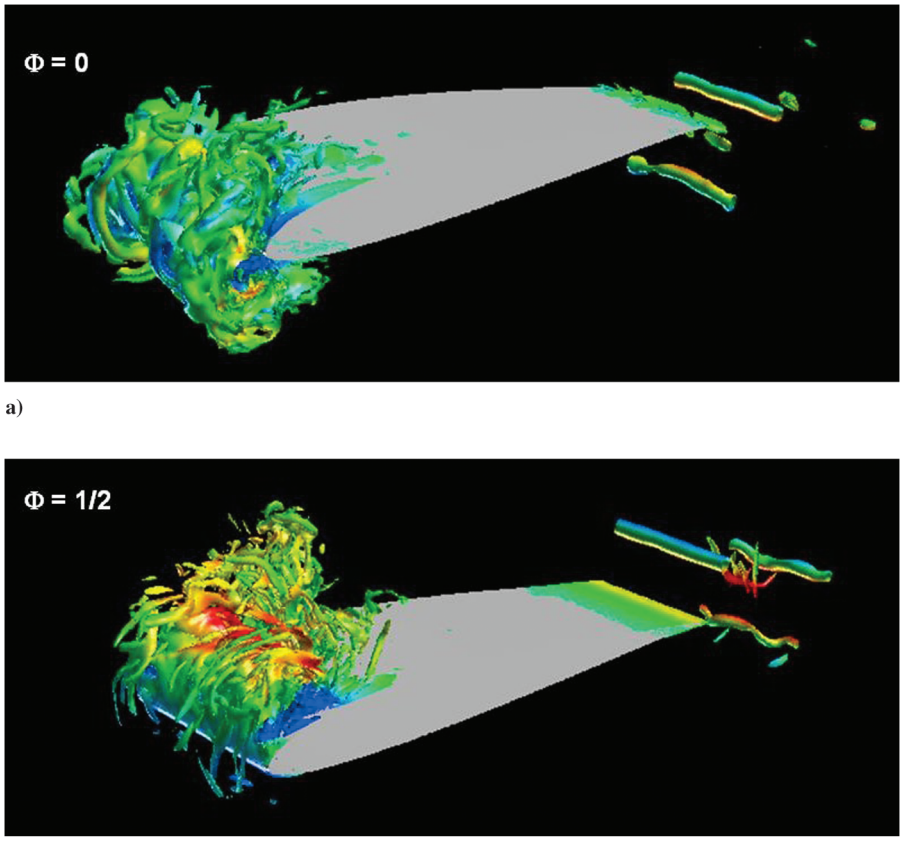

Fig. 24 Isosurfaces of instantaneous vorticity magnitude showing breakdown of leading-edge vortex system, $\alpha_o = 14°$, $Re_c = 10^4$, $k = 10$ and $h_o = 0.04$.

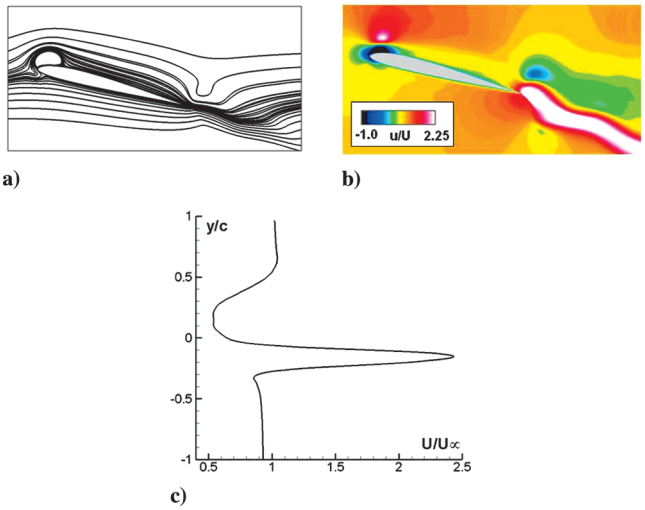

Fig. 25 Time-averaged flow structure for high-frequency, small-amplitude plunging, $\alpha_o = 14°$, $Re_c = 10^4$, $k = 10$ and $h_o = 0.04$. (a) streamline pattern, (b) streamwise velocity contours, and (c) streamwise velocity profile in the near wake at $x/c = 1.8$.

the near wake is closely aligned with the general freestream direction. The strong vortices shed at the trailing edge also exhibit an arrangement corresponding to a jet rather than a wake, as demonstrated later.

The most intriguing behavior takes place near the airfoil leading edge. As the airfoil plunges in the downward direction (Fig. 22c), leading-edge separation and vortex formation occurs on the airfoil upper surface. This is more clearly seen in the phase-averaged representation (Fig. 23c) because, in the corresponding instantaneous plot, the vortex is surrounded by remnants of the broken down vortices generated in the previous cycle. As the airfoil moves in the upward direction (Figs. 22d and 23d), the large negative motion-induced angle of attack (-24.6 deg at $\Phi = \frac{3}{4}$) forces the dynamic-stall vortex to propagate backward around the leading edge. At the top of the stroke (Fig. 23a), the vortex is in front of the airfoil leading edge, and another dynamic-stall vortex (of opposite-signed vorticity) is generated on the lower surface. This leading-edge vortex pair experiences a dramatic breakdown as it impinges against the airfoil, as seen in Fig. 22b. This partially disintegrated vortex system wraps around the new vortex being formed above the airfoil during the next cycle (Fig. 22c) and eventually propagates along the airfoil. Given the explosive spanwise breakdown of the leading-edge vortex system, the phase-averaged flow displays no coherent vortices convecting above the airfoil, as was the case for smaller plunging amplitudes (Figs. 21g and 21h).

The instantaneous three-dimensional flow structure is displayed in Fig. 24 using an isosurface of vorticity magnitude. The frame corresponding to the top of the stroke (Fig. 24a), shows the complex transitional leading-edge vortex system as it moves in front of the airfoil. At the bottom of the stroke (Fig. 24b), the stretched vortex filaments from the broken down leading-edge vortex system are observed to wrap around the new dynamic-stall vortex being generated above the airfoil. The coherent vortices shed from the trailing edge are also observed in these pictures.

The time-averaged flow structure for $h_o = 0.04$ is displayed in Fig. 25. The mean streamline pattern is characterized by a closed leading-edge recirculation region or trapped vortex. However, downstream of this bubble, the flow is fully attached. The velocity contours in the near-wake region exhibit a very strong jet associated with the coherent vortices shed at the sharp trailing edge (seen, for instance, in Fig. 23d). This is demonstrated more clearly in the plot of the streamwise velocity component at the station $x/c = 1.8$, where a maximum jet velocity of order $2.5U_\infty$ is observed.

Finally, the effect of oscillation amplitude on the computed mean drag coefficient for $Re_c = 10^4$ is summarized in Table 3. Even for the smallest amplitude ($h_o = 0.005$), there is a reduction of approximately 35% in C_D. For $h_o = 0.025$, the drag coefficient is nearly zero and becomes negative (i.e., implying thrust) for the highest amplitude. This significant net thrust is associated with the strong jet previously noted in reference to Fig. 25.

V. Conclusions

An implicit large-eddy simulation approach was applied to the prediction of transitional flows over plunging airfoils at low Reynolds number relevant to micro air vehicles. This ILES method is found to be particularly attractive for the present flows exhibiting mixed laminar, transitional, and turbulent regions. Both 2-D and 3-D simulations were performed for an SD7003 airfoil section plunging at relatively high frequency k and small amplitude.

The first case corresponds to the following conditions: static angle of attack $\alpha_o = 4$ deg, reduced frequency $k = 3.93$, and plunging amplitude $h_o = 0.05$. The Reynolds number based on airfoil chord ranged from $Re_c = 10^3$ to $Re_c = 4 \times 10^4$. At $Re_c = 10^4$, the effect of transition was found to be limited. In particular, the dynamic-stall vortex system generated near the leading edge retains its coherence as it propagates downstream close to the surface of the airfoil. Minor spanwise instability effects are found in the secondary vorticity ejected from the surface. For $Re_c = 4 \times 10^4$, the dynamic-stall vortex system is initially laminar and two-dimensional in character. However, it subsequently exhibits an abrupt breakdown due to spanwise instability effects. This 3-D process of transition is described for the first time and is found to involve the almost simultaneous collapse of both the primary and secondary laminar vortical structures. The dramatic breakdown and vorticity cancellation manifests in a rapid reduction of the maximum values of phase-averaged vorticity. The phase-averaged computed flows are found to be in fairly good agreement with experimental measurements. Despite the significant differences in vortical structure, the computed lift is found to be fairly insensitive to Reynolds number and is in agreement with inviscid theory. This is due to the fact that lift is dominated by noncirculatory effects at this relatively high value of reduced frequency. The mean drag coefficient decreases significantly with increasing Reynolds number and becomes negative (implying thrust) for both $Re_c = 10^4$ and 4×10^4.

The second case dealt with the suppression of stall using small-amplitude high-frequency plunging oscillations. The initial static flow at $\alpha_o = 14$ deg was fully stalled. Plunging oscillations with frequency $k = 10$ and amplitude $h_o = 0.005$ were then imposed to diminish separation. For $Re_c = 6 \times 10^4$, stall is completely eliminated by the high-frequency forcing, and the mean flow is essentially attached. The instantaneous flow structure is characterized by the formation of coherent dynamic-stall-like vortices which are generated near the leading edge due to the large motion-induced angle of attack. These vortices propagate close to the airfoil surface and quickly transition due to the onset of spanwise instabilities. The present results demonstrate that low-Reynolds-number flows are quite receptive to either imposed or unintended vibrations. This property could be exploited in small and micro air vehicles through either suitable actuation or aeroelastic tailoring. At a lower Reynolds number ($Re_c = 10^4$), control effectiveness diminishes, and separation (although substantially reduced) is not completely eliminated. To enhance control effectiveness at lower Re_c, the plunging amplitude was increased. For $h_o = 0.04$, the dynamic-stall vortex system is observed to move in front and around the airfoil leading edge and experiences an abrupt breakdown. Therefore, in this intriguing new flow regime, a regular train of vortices convecting over the airfoil is no longer observed in the phase-averaged representation. The corresponding time-averaged flow structure in the near-wake region displays a very strong jet with maximum velocities in excess of twice the freestream value.

This investigation demonstrates the critical role of transition on the unsteady flows over maneuvering airfoils even for moderate Reynolds numbers. The complex mixed laminar-turbulent flow structures which emerge, although amenable to simulation by the present ILES methodology, represent a formidable challenge for more efficient reduced-order approaches incorporating simplified

transition models. Finally, complementary high-resolution experimental measurements of the transitional dynamic-stall vortex system are required.

Acknowledgments

This work was supported in part by U.S. Air Force Office of Scientific Research under a task monitored by J. Schmisseur, and by a grant of high-performance computing time from the Department of Defense High-Performance Computing Shared Resource Center at the U.S. Air Force Research Laboratory. The author is grateful to M. Ol for providing his experimental data, to V. Golubev for help with his program to compute the theoretical loads, to P. Morgan for his assistance with grid generation, and to S. Sherer for his help with the high-order overset tools for FDL3DI.

References

[1] Mueller, T. J., "Low Reynolds Number Vehicles," AGARDograph No. 288, 1985.

[2] Shyy, W., *Aerodynamics of Low Reynolds Number Flyers*, Cambridge Univ. Press, Cambridge, England, U.K., 2008.

[3] Ol, M. V., McAuliffe, B. R., Hanff, E. S., Scholz, U., and Khler, C., "Comparison of Laminar Separation Bubble Measurements on a Low Reynolds Number Airfoil in Three Facilities," AIAA Paper 2005-5149, June 2005.

[4] Radespiel, R., Windte, J., and Scholz, U., "Numerical and Experimental Flow Analysis of Moving Airfoils with Laminar Separation Bubbles," AIAA Paper 2006-501, Jan. 2006.

[5] Yuan, W., Khalid, M., Windte, J., Scholz, U., and Radespiel, R., "An Investigation of Low-Reynolds-Number Flows past Airfoils," AIAA Paper 2005-4607, June 2005.

[6] Galbraith, M., and Visbal, M., "Implicit Large Eddy Simulation of Low Reynolds Number Flow past the SD7003 Airfoil," AIAA Paper 2008-0225, Jan. 2008.

[7] McGowan, G., Gopalarathnam, A., OL, M., Edwards, J., and Fredberg, D., "Computation vs. Experiment for High-Frequency Low-Reynolds-Number Airfoil in Pitch and Plunge," AIAA Paper 2008-0653, Jan. 2008.

[8] Visbal, M. R., and Rizzetta, D. P., "Large-Eddy Simulation on Curvilinear Grids Using Compact Differencing and Filtering Schemes," *Journal of Fluids Engineering*, Vol. 124, No. 4, 2002, pp. 836–847. doi:10.1115/1.1517564

[9] Visbal, M. R., Morgan, P. E., and Rizzetta, D. P., "An Implicit LES Approach Based on High-Order Compact Differencing and Filtering Schemes," AIAA Paper 2003-4098, June 2003.

[10] Koochesfahani, M., "Vortical Patterns in the Wake of an Oscillating Airfoil," *AIAA Journal*, Vol. 27, No. 9, 1989, pp. 1200–1205. doi:10.2514/3.10246

[11] Lai, J. C. S., and Platzer, M. F., "Jet Characteristics of a Plunging Airfoil," *AIAA Journal*, Vol. 37, No. 12, 1999, pp. 1529–1537. doi:10.2514/2.641

[12] Cleaver, D. J., Wang, Z., and Gursul, I., "Delay of Stall by Small Amplitude Airfoil Oscillations at Low Reynolds Number," AIAA Paper 2009-392, Jan. 2009.

[13] Carr, L., "Progress in Analysis and Prediction of Dynamic Stall," *Journal of Aircraft*, Vol. 25, No. 1, 1988, pp. 6–17. doi:10.2514/3.45534

[14] Visbal, M. R., and Shang, J. S., "Investigation of the Flow Structure Around a Rapidly Pitching Airfoil," *AIAA Journal*, Vol. 27, No. 8, 1989, pp. 1044–1051. doi:10.2514/3.10219

[15] Visbal, M. R., "On the Formation and Control of the Dynamic Stall Vortex on a Pitching Airfoil," AIAA Paper 1991-0006, Jan. 1991.

[16] Choudhuri, P. G., Knight, D. D., and Visbal, M. R., "Two-Dimensional Unsteady Leading-Edge Separation on a Pitching Airfoil," *AIAA Journal*, Vol. 32, No. 4, 1994, pp. 673–681. doi:10.2514/3.12040

[17] Visbal, M. R., "Dynamic Stall of a Constant-Rate Pitching Airfoil," *Journal of Aircraft*, Vol. 27, No. 5, 1990, pp. 400–407. doi:10.2514/3.25289

[18] Ekaterinaris, J., and Platzer, M., "Computational Prediction of Airfoil Dynamic Stall," *Progress in Aerospace Sciences*, Vol. 33, Nos. 11–12, 1998, pp. 759–846. doi:10.1016/S0376-0421(97)00012-2

[19] Vinokur, M., "Conservation Equations of Gasdynamics in Curvilinear Coordinate Systems," *Journal of Computational Physics*, Vol. 14, No. 2, 1974, pp. 105–125. doi:10.1016/0021-9991(74)90008-4

[20] Steger, J. L., "Implicit Finite-Difference Simulation of Flow About Arbitrary Two-Dimensional Geometries," *AIAA Journal*, Vol. 16, No. 7, 1978, pp. 679–686. doi:10.2514/3.7377

[21] Anderson, D. A., Tannehill, J. C., and Pletcher, R. H., *Computational Fluid Mechanics and Heat Transfer*, McGraw–Hill, New York, 1984.

[22] Stolz, S., and Adams, N., "An Approximate Deconvolution Procedure for Large-Eddy Simulation," *Physics of Fluids*, Vol. 11, No. 7, 1999, pp. 1699–1701. doi:10.1063/1.869867

[23] Mathew, J., Lechner, R., Foysi, H., Sesterhenn, J., and Friedrich, R., "An Explicit Filtering Method for LES of Compressible Flows," *Physics of Fluids*, Vol. 15, No. 8, 2003, pp. 2279–2289. doi:10.1063/1.1586271

[24] Visbal, M. R., and Gaitonde, D. V., "High-Order Accurate Methods for Complex Unsteady Subsonic Flows," *AIAA Journal*, Vol. 37, No. 10, 1999, pp. 1231–1239. doi:10.2514/2.591

[25] Gaitonde, D. V., and Visbal, M. R., "High-Order Schemes for Navier–Stokes Equations: Algorithm and Implementation into FDL3DI," Air Force Research Lab. Technical Rept. AFRL-VA-WP-TR-1998-3060, 1998.

[26] Lele, S. K., "Compact Finite Difference Schemes with Spectral-like Resolution," *Journal of Computational Physics*, Vol. 103, No. 1, 1992, pp. 16–42. doi:10.1016/0021-9991(92)90324-R

[27] Visbal, M. R., and Gaitonde, D. V., "On the Use of High-Order Finite-Difference Schemes on Curvilinear and Deforming Meshes," *Journal of Computational Physics*, Vol. 181, No. 1, 2002, pp. 155–185. doi:10.1006/jcph.2002.7117

[28] Gaitonde, D. V., Shang, J. S., and Young, J. L., "Practical Aspects of Higher-Order Numerical Schemes for Wave Propagation Phenomena," *International Journal for Numerical Methods in Engineering*, Vol. 45, No. 12, 1999, pp. 1849–1869. doi:10.1002/(SICI)1097-0207(19990830)45:12<1849::AID-NME657>3.0.CO;2-4

[29] Alpert, P., "Implicit Filtering in Conjunction with Explicit Filtering," *Journal of Computational Physics*, Vol. 44, No. 1, 1981, pp. 212–219. doi:10.1016/0021-9991(81)90047-4

[30] Gaitonde, D. V., and Visbal, M. R., "Further Development of a Navier–Stokes Solution Procedure Based on Higher-Order Formulas," AIAA Paper 99-0557, Jan. 1999.

[31] Morgan, P. E., Visbal, M. R., and Rizzetta, D. P., "A Parallel High-Order Flow Solver for Large-Eddy and Direct Numerical Simulation," AIAA Paper 2002-3123, June 2002.

[32] Sherer, S., and Visbal, M., "Implicit Large Eddy Simulations Using a High-Order Overset Grid Solver," AIAA Paper 2004-2530, June 2004.

[33] Visbal, M., and Gaitonde, D., "Very High-Order Spatially Implicit Schemes for Computational Acoustics on Curvilinear Meshes," *Journal of Computational Acoustics*, Vol. 9, No. 4, 2001, pp. 1259–1286.

[34] Fung, Y. C., *An Introduction to the Theory of Aeroelasticity*, Dover, New York, 1993.

[35] Glezer, A., Amitay, M., and Honohan, A., "Aspects of Low- and High-Frequency Actuation for Aerodynamic Flow control," *AIAA Journal*, Vol. 43, No. 7, 2005, pp. 1501–1511. doi:10.2514/1.7411

[36] Visbal, M., Gaitonde, D., and Roy, S., "Control of Transitional and Turbulent Flows Using Plasma-Based Actuators," AIAA Paper 2006-3230, June 2006.

P. Givi
Associate Editor